IEEE Access
Multidisciplinary ⋮ Rapid Review ⋮ Open Access Journal

Received 4 March 2024, accepted 17 March 2024, date of publication 25 March 2024, date of current version 29 March 2024.

Digital Object Identifier 10.1109/ACCESS.2024.3381526

APPLIED RESEARCH

Enhancing Grid Stability Using a Virtual Inertia-Integrated Railway Power Conditioner in Railway Power Supplies With High Renewable Energy Penetration

TEERAPHON PHOPHONGVIWAT[1], (Member, IEEE), THUNWA BOONLERT[2], (Student Member, IEEE), AND KOMSAN HONGESOMBUT[2], (Member, IEEE)

[1]Department of Electrical Engineering, School of Engineering, King Mongkut's Institute of Technology Ladkrabang, Bangkok 10520, Thailand
[2]Department of Electrical Engineering, Faculty of Engineering, Kasetsart University, Bangkok 10900, Thailand

Corresponding author: Komsan Hongesombut (fengksh@ku.ac.th)

This work was supported by the King Mongkut's Institute of Technology Ladkrabang under Grant 2565-02-010-034.

ABSTRACT As electric power systems increasingly integrate Renewable Energy Sources (RESs), the consequent reduction in system inertia has heightened their sensitivity to disturbances, such as sudden load changes. This issue is especially relevant in railway power supply systems, which are evolving to be dominated by RESs. Traditional solutions, including Railway Power Conditioners (RPCs), primarily address unbalanced loads and reactive power compensation but offer limited frequency support. This paper introduces a Virtual Inertia-Integrated Railway Power Conditioner (VIIRPC), a novel solution that enhances traditional RPCs with Energy Storage Systems (ESS) to provide critical virtual inertia support, thereby addressing the critical gap in frequency stability amidst the evolving energy landscape of railway systems. Utilizing a current source-based model, the VIIRPC effectively extends inertia support from two-phase systems to balanced three-phase systems at the Point of Common Coupling (PCC). This achievement is realized by dividing a virtual inertia signal and integrating it into both sides of the RPC control loop, while respecting each side's signal orientation. Simulations have been conducted to verify the operation under different loading conditions, including a 4-minute headway train schedule, under both conventional and low-inertia grid conditions. These results demonstrate that the VIIRPC outperforms traditional RPCs by enhancing frequency stability and maintaining conventional functionalities. This advancement is particularly significant for modern, RES-dominated railway power supplies, especially in remote areas with RES-based power sources and low short-circuit levels at the PCC.

INDEX TERMS Virtual inertia control, railway power conditioners, unbalanced power systems, Scott transformers, renewable energy sources.

NOMENCLATURE

A. ABBREVIATIONS

arr.	Arrive.
AT	Autotransformers.
BI-phase	Two-phase systems in PowerFactory.
DD mode	Autotransformer mode in PowerFactory.
dep.	Depart.
ESS	Energy Storage System.
MVA_{sc}	Short-circuit level at the observed bus.
PCC	Point of Common Coupling.
pf	Power Factor.

The associate editor coordinating the review of this manuscript and approving it for publication was Ton Duc Do.

RES	Renewable Energy Source.
RoCoF	Rate of Change of Frequency.
RPC	Railway Power Conditioner.
TPSS	Traction Power Substation.
u_k	Transformer short-circuit impedance voltage.
VIIRPC	Virtual Inertia-Integrated Railway Power Conditioner.
VUF	Voltage Unbalance Factor.

B. SYMBOLS

d_{ik}	Length between conductor *i-th* to *k-th*.
d'_{ik}	Length between conductor *i-th* to equivalent conductor *i-th* under earth's surface.
D	Damping coefficient.
D_{VI}	Virtual damping gain.
f	Measured frequency.
f_0	Reference frequency.
h_i	Length between conductor *i-th* to earth.
$\boldsymbol{i_{dyn}}$	Dynamic current.
$\boldsymbol{i_L}$	Load current.
$\boldsymbol{i_s}$	Static current.
J	Rotor's moment of inertia.
K	The compensation factor.
K_{VI}	Virtual inertia gain.
P_e	Electrical power.
P_m	Mechanical power.
P_α	Active power load measured at the α phase.
P_β	Active power load measured at the β phase.
Q_α	Reactive power load measured at the α phase.
Q_β	Reactive power load measured at the β phase.
r_i	Radius of conductor *i-th*.
R_{VI}	Virtual inertia droop gain.
$\boldsymbol{S^*_{dyn}}$	Apparent power conjugate.
T_e	Electrical torque.
T_m	Mechanical torque.
$\boldsymbol{u^*}$	Voltage conjugate.
$\boldsymbol{Y_{load}}$	Load admittance.
$\boldsymbol{z_{Eii}}$	Self-earth impedance.
$\boldsymbol{z_{Eij}}$	Mutual earth impedance.
$\boldsymbol{z_{Gii}}$	Self-geometrical impedance.
$\boldsymbol{z_{Gij}}$	Mutual geometrical impedance.
$\boldsymbol{z_{ii}}$	Self-impedance.
$\boldsymbol{z_{ij}}$	Mutual impedance.
$\boldsymbol{z_{Lii}}$	Internal impedance.
μ_0	Vacuum magnetic permeability.
ω_s	The nominal angular speed.
Δf	Frequency different.
ΔP_{RPC}	RPC's transferring active power
ΔP_{VI}	Virtual inertia power.
$\Delta Q_{\alpha,out}$	Reactive power injection of the α phase.
$\Delta Q_{\beta,out}$	Reactive power injection at the β phase.
$\Delta\delta_m$	Rotor angle difference.
$\Delta\omega_m$	Angular speed difference.

I. INTRODUCTION

The integration of renewable energy sources is significantly transforming railway power supply systems. This transformation involves a shift from traditional synchronous generators to more inverter-based generations. This shift is significant because traditional synchronous generators contribute to the inertia of power system, which is crucial for maintaining frequency stability [1]. The research challenge emerges in scenarios where the traction power substation (TPSS) predominantly relies on renewable energy sources (RESs). Inverter-based generation systems are unable to provide as much short-circuit current as synchronous generators. Consequently, the short-circuit level at the point of common coupling (PCC) of the TPSS, which is related to the source impedance, becomes constrained and lower than in power grids with a high presence of synchronous generators. The reduction in short-circuit capacity, leading to an increase in source impedance, can result in power quality challenges, including voltage fluctuations, especially during fault conditions or transient disturbances. Furthermore, in contemporary power systems, the integration of inverter-based generation sources, such as wind farms and solar farms, does not contribute physical inertia that is characteristic of traditional rotating synchronous generators. This shift leads to a reduction in the overall inertia of the power grid, necessitating advanced control strategies to maintain system frequency stability. To compensate for the absence of inertia, the introduction of virtual inertia control has been made to enhance the stability of the grid. The kinetic energy stored in rotating mass is emulated by this control technique through the utilization of Energy Storage Systems (ESS). A comprehensive review of virtual inertia control techniques has been conducted in [2]. These methods often involve the use of ESS, especially Battery Energy Storage Systems (BESS), to emulate the kinetic energy of rotor systems traditionally found in synchronous generators [3], [4]. The application of BESS in modern power systems can be expanded to develop Peer-to-Peer (P2P) markets, as reviewed in [5], [6], and [7]. Certain research suggests the implementation of virtual inertia without depending on BESS. This approach involves using a reduced generation margin for power reserves, offering a cost-effective alternative [8], [9]. While most research has focused on the generation side of inertia, there is an emerging interest in demand-side approaches. These approaches involve smart load management, offering new perspectives and solutions in the domain of power system stability [10].

In modern railway power supply systems, upon the arrival of trains at the TPSS, unbalanced loads and frequency deviations are inevitable. Therefore, the need for more intelligent, flexible, and intricate systems to accommodate the dynamic nature of railway operations [11]. Several studies propose various methods to incorporate frequency control in railway systems. These techniques are crucial for maintaining the stability and efficiency of railway operations, especially in high-speed railways [12], [13], [14]. The coordination of electric train operations for primary control is discussed in [12] and

TABLE 1. Research gap demonstration.

Research	Approach	Frequency stability	Voltage fluctuation	Unbalanced factor	Power factor
[12, 13]	Using Train schedule managing	✓	×	×	×
[14]	Controlling traction motors	✓	×	×	×
[18] – [21]	Using RPC based approach	×	×	✓	✓
This research	Using VIIRPC	✓	✓	✓	✓

[13]. Meanwhile, [14] proposes a feedback-linearized virtual inertia control (VIC) strategy for the train's traction converter, based on a sliding mode observer (SMO), which is discussed to mitigate low-frequency oscillation (LFO) in the system. It has been observed that recent developments in frequency control have emphasized virtual inertia techniques. Apart from the virtual inertia techniques described in [12], [13], and [14], the potential integration of virtual inertia control into railway power conditioners is recognized.

Introduced in 1993, the Railway Power Conditioner (RPC) has been principally designed to balance the secondary side of traction transformers by regulating the power demand across different load phases [15] and [16]. In addition to load balancing, RPC also improves power quality by providing reactive power compensation and harmonic suppression [17]. Various methodologies for reactive compensation, applicable to different traction transformer configurations, have been introduced in the literature. Specifically, a method for fractional reactive power compensation tailored for V/V transformers is proposed in [18]. Following this, strategies for reactive power compensation in YNvd-connected balanced transformers have been advanced, as detailed in [19] and [20]. The active power quality compensator (APQC) system, which compensates for reactive power, negative sequences, and harmonics, is highlighted [21]. RPC topologies and operational modes are detailed in [22]. Furthermore, heavy traction loads, particularly from high-speed trains, can generate significant reverse power during braking. In Japan, the installation of a BESS at the DC link of the RPC at Ushiku Sectioning Post on the Joban Line has been reported, facilitating the capture of this excess power [23]. Alternatively, a Supercapacitor-Based Energy Storage System (SCESS) can be incorporated at the DC link of the RPC, serving to both recycle regenerative braking energy and enhance power quality. Supercapacitors provide benefits such as higher energy density and faster response times [24]. A technical-economic model for designing RPC-based ESS, focusing on regenerative braking energy recycling applications, has also been developed [25].

While much of the existing literature focuses on energy management and frequency regulation in railways through train operation coordination or enhanced traction control loops, the potential of using an RPC with ESS at TPSS for frequency regulation has been less discussed in academic research. To bridge this gap, this study proposes the integration of ESS with RPC to provide virtual inertia services for frequency support. The virtual inertia-integrated railway power conditioner (VIIRPC) developed in this study combines the conventional RPC control loop with a virtual inertia control loop. While the RPC loop balances active power and compensates for the reactive power of traction loads at the traction transformer's secondary side, the virtual inertia loop provides an inertial response to mitigate traction loads' ramp rate. The VIIRPC's capability to provide virtual inertia services is promising for tackling challenges in TPSS in remote areas, predominantly dependent on RESs, where load frequency regulation and load balancing are crucial. This integrated solution enhances frequency support and ensures a more balanced power supply in such systems. The research gap is summarized in Table 1.

In this study, simulations and their corresponding models are developed using the PowerFactory software. A series of simulation scenarios are presented to validate the VIIRPC's functionality and to demonstrate its performance under a train schedule load characteristic. The significant contributions of this paper are summarized as follows:

- This paper proposes a novel concept of utilizing RPC for frequency support by integrating virtual inertia functionality.
- It also presents a simplified and comprehensive model for the VIIRPC. This model employs a current source-based framework for the RPC, enhanced with an integrated virtual inertia control mechanism, making it particularly advantageous for conducting power system stability studies in railway power supply systems.
- Additionally, this paper proposes integrating the VIIRPC into TPSS. The VIIRPC introduces inertia support, transitioning from two-phase systems using a Scott transformer to balanced three-phase systems. This integration enables more efficient deployment of TPSS in remote areas that primarily rely on RESs.

The organization of this paper is outlined as follows: Section II offers a detailed description of the system configuration, focusing on the 2 × 25 kV autotransformer (AT) feeding system and its components. Section III introduces the proposed control strategy, VIIPRC, and evaluative criteria. Section IV explains case studies, discusses the simulation outcomes for each case study. Section V offers concluding remarks and summarizes the findings.

II. SYSTEM OVERVIEW AND MODELING

The research challenge is defined by the situation in which the TPSS is supplied by a 115 kV power grid dominated

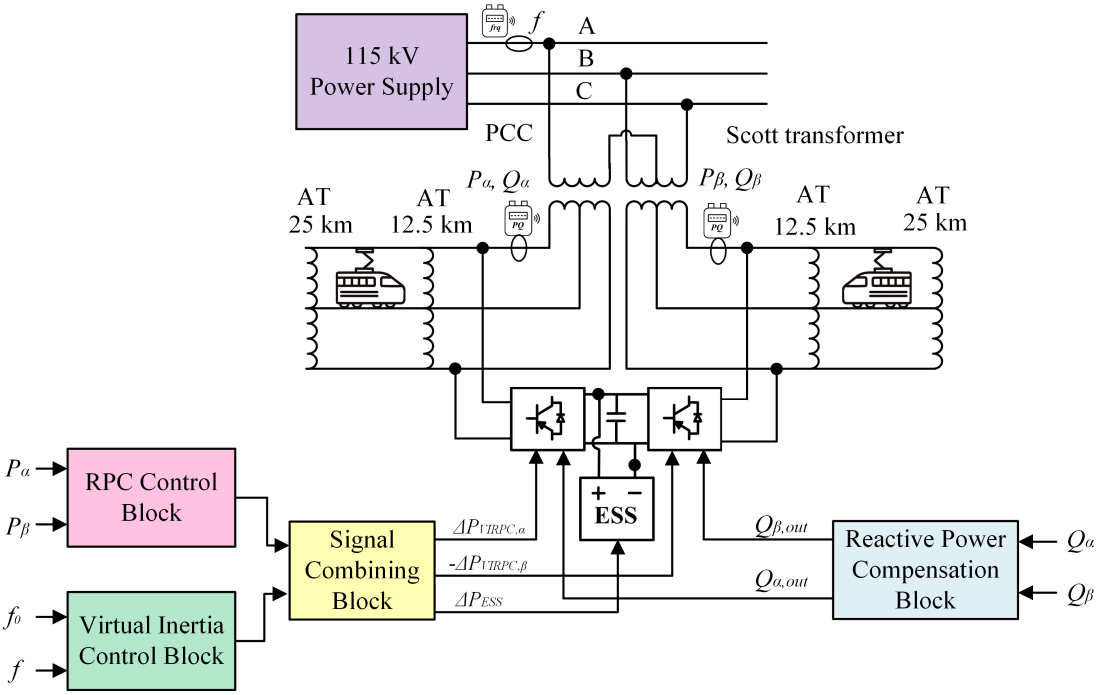

FIGURE 1. The system configuration.

by RESs. Since inverter-based generation cannot provide as much short-circuit current as a synchronous generator, the short-circuit level at the point of common coupling (PCC) of this TPSS is limited and lower than that in power grids dominated by synchronous generators. This leads to a reduction in the overall inertia of the power grid. Therefore, when the train arrives at this TPSS, higher unbalanced loads and frequency deviations become inevitable. The system configuration overview is shown in Fig. 1. The modeling of each component is described in the following subsections.

A. THE LOW-INERTIA POWER SYSTEM MODEL

As the penetration of RESs disrupts electricity utilities, electrified railway systems are also affected by this transition. In the real world, the operating frequency of power systems can vary within an acceptable range, as defined in the grid code. Frequency deviation is caused by imbalances between demand and supply, where changes in active power result in proportional frequency variations, expressed in (1) and (2). The moment of inertia (J) plays a crucial role in frequency regulation, reducing the rate of change of frequency (RoCoF) during the initial seconds of a disturbance. Subsequently, the control strategy takes charge of restoring the frequency to its nominal value. The reduction in inertia leads to a rapid frequency change during power mismatches, triggering under or over-frequency relays that command protection devices to trip out. This scenario can cause instability in a modern power system due to RES domination.

$$T_m - T_e = J \cdot \frac{d^2 \Delta\delta_m}{dt} + D \cdot \frac{d\,\Delta\delta_m}{dt} \tag{1}$$

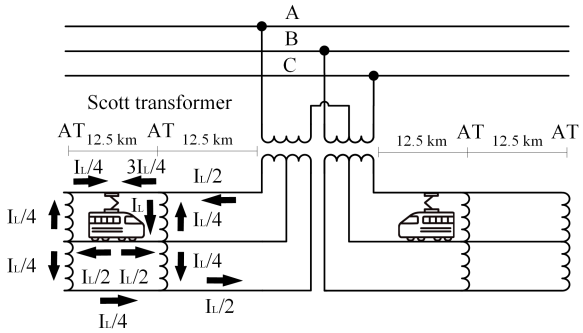

FIGURE 2. The 2 × 25 kV AT feeding systems.

$$P_m - P_e = \frac{J}{\omega_s} \cdot \frac{d\,\Delta\omega_m}{dt} + D\Delta\omega_m \tag{2}$$

where T_m is the mechanical torque, T_e is the electrical torque, P_m is mechanical power, P_e is electrical power, J is the rotor's moment of inertia, D is a damping coefficient, $\Delta\delta_m$ is rotor angle difference, ω_s is the nominal angular speed, and $\Delta\omega_m$ is angular speed difference.

In this study, the 115-kV power supply of Fig. 1 is modeled using the equivalent of a generator, based on (1) and (2).

B. THE 2 × 25 kV AT FEEDING SYSTEM AND AUTOTRANSFORMER MODEL

In this study, the 2 × 25 kV AT feeding system is adopted, as shown in Fig. 2, due to its significant advantages in modern railway power supply systems. This system requires fewer transformer installations, spaced 12.5 km apart, effectively

TABLE 2. The parameters of autotransformer model.

Parameters	Values
Rated Capacity (MVA)	30
Rated Voltage (kV)	50:25
Copper loss (kW)	0
u_k (%)	1%

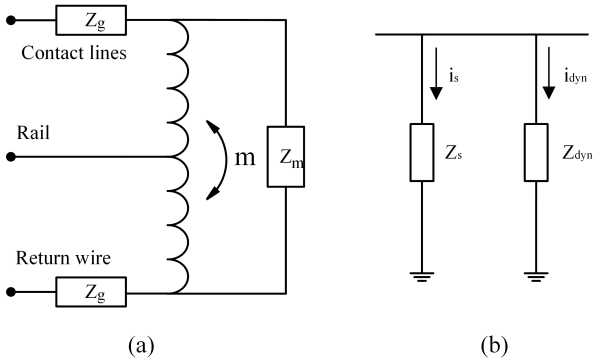

FIGURE 3. Railway system models a) The autotransformer diagram b) The traction load.

reducing construction costs and mitigating electromagnetic interference. Additionally, this system improves efficiency by halving the return current to the substation, leading to lower voltage drop and power loss in the conductors.

Autotransformers are integrated by establishing connections to both +25 kV and -25 kV terminals. The center tab of these transformers is linked to the railway tracks to enable the conduction of return current. Fig. 3 (a) illustrates a diagram of the autotransformer. A mathematical model of this transformer has been suggested in [26] and can be encapsulated through (3) where z_g is conductor's impedance, and z_m is mutual impedance.

In this paper, autotransformers are modeled by using a single-phase transformer in a DD mode (Autotransformer connection in PowerFactory, [27]). The specification is shown in Table 2, which is adapted from [28].

$$\mathbf{Y_{AT}} = \begin{bmatrix} \frac{1}{2z_g} + \frac{1}{z_m+2z_g} & \frac{-1}{z_g} & \frac{1}{2z_g} - \frac{1}{z_m+2z_g} \\ \frac{-1}{z_g} & \frac{2}{z_g} & \frac{-1}{z_g} \\ \frac{1}{2z_g} - \frac{1}{z_m+2z_g} & \frac{-1}{z_g} & \frac{1}{2z_g} + \frac{1}{z_m+2z_g} \end{bmatrix} \tag{3}$$

C. THE TRACTION LOAD MODEL

A single-phase traction load can be considered as a power-controlled current load. To connect with railway systems, the BI-phase technology (Two-phase systems, in PowerFactory) is necessary. The load model in dynamic simulations, as shown in Fig. 3 (b), comprises a static part and a dynamic part, represented in (4) to (6) and documented in [29].

$$\boldsymbol{i_L} = \boldsymbol{i_s} + \boldsymbol{i_{dyn}} \tag{4}$$

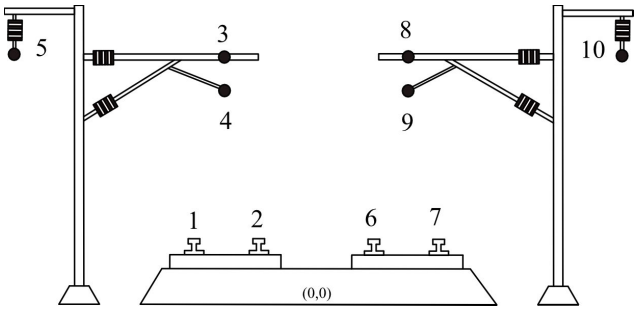

FIGURE 4. The cross-section geometry of 2 × 25 kV catenary systems.

$$\boldsymbol{i_s} = \boldsymbol{Y_{load}}\boldsymbol{u} \tag{5}$$

$$\boldsymbol{i_{dyn}} = \frac{\boldsymbol{S^*_{dyn}}}{\boldsymbol{u^*}} \tag{6}$$

where $\boldsymbol{i_L}$ is load current, $\boldsymbol{i_s}$ is static current, $\boldsymbol{i_{dyn}}$ is dynamic current, $\boldsymbol{Y_{load}}$ is load admittance, $\boldsymbol{S^*_{dyn}}$ is apparent power conjugate, and $\boldsymbol{u^*}$ is voltage conjugate.

D. THE MULTI-CONDUCTOR MODEL

The self and mutual coupling of each conductor can be modeled using the "Line Constants or Line Couplings Model" in PowerFactory. This model encompasses three components: internal impedance, geometrical impedance, and an earth correction term. The geometrical term can be described by equations (7) through (11), which apply the catenary geometry as shown in Fig. 4. Additional details regarding the other components can be found in [30]. The geometry of the catenary system and the impedance matrices, which are expressed in meters and ohms per kilometer respectively for this model, are shown in the Appendix.

$$\mathbf{Z_{line}} = \begin{bmatrix} z_{11} & z_{12} & \cdots & \cdots & z_{1n} \\ z_{21} & \ddots & \cdots & \cdots & z_{2n} \\ \vdots & \vdots & z_{ii} & z_{ik} & \vdots \\ \vdots & \vdots & z_{ki} & z_{kk} & \vdots \\ z_{n1} & z_{n2} & \cdots & \cdots & z_{nn} \end{bmatrix}_{n\times n} \tag{7}$$

$$z_{ii} = z_{Lii} + z_{Gii} + z_{Eii} \tag{8}$$

$$z_{ij} = z_{Gij} + z_{Eij} \tag{9}$$

$$z_{Gii} = j\omega \cdot \frac{\mu_0}{2\pi} \cdot ln\frac{2h_i}{r_i} \tag{10}$$

$$z_{Gik} = j\omega \cdot \frac{\mu_0}{2\pi} \cdot ln\frac{d'_{ik}}{d_{ik}} \tag{11}$$

From (7)-(11), z_{ii} is self-impedance, z_{ij} is mutual impedance, z_{Lii} is internal impedance, z_{Gii} is self-geometrical impedance, z_{Eii} is self-earth impedance, z_{Gij} is mutual geometrical impedance, z_{Eij} is mutual earth impedance, ω is angular speed, μ_0 is vacuum magnetic permeability, h_i is length between conductor *i-th* to earth, r_i is radius of conductor *i-th*, d'_{ik} is length between conductor *i-th* to equivalent conductor *i-th* under earth's surface, and d_{ik} is length between conductor *i-th* to *k-th*.

E. THE SCOTT TRANSFORMER MODEL

A traction transformer is necessary to convert the three-phase system to two single-phase systems, which can then supply the traction loads for each supply feeder. Scott transformers are one of the well-known transformer types for this application in electrified railway systems. The diagram of the Scott transformer is illustrated in Fig. 5.

Consider the α phase corresponding to the teaser winding, and the β phase corresponding to the main winding. The turn ratios of the Scott connection for the α phase and β phase are $\sqrt{3}/2 : 2$ and $k{:}2$, respectively. The model for the Scott transformer, as described in [31], can be expressed (12) to (19).

$$\begin{bmatrix} \mathbf{I_P} \\ \mathbf{I_S} \end{bmatrix} = \begin{bmatrix} \mathbf{Y_{PP}} & \mathbf{Y_{PS}} \\ \mathbf{Y_{PS}^T} & \mathbf{Y_{SS}} \end{bmatrix} = \mathbf{Y_{scott}} \begin{bmatrix} \mathbf{V_P} \\ \mathbf{V_S} \end{bmatrix} \tag{12}$$

$$\mathbf{I_P} = \begin{bmatrix} I_A & I_B & I_C \end{bmatrix} \tag{13}$$

$$\mathbf{V_P} = \begin{bmatrix} V_A & V_B & V_C \end{bmatrix} \tag{14}$$

$$\mathbf{I_S} = \begin{bmatrix} I_T^{\alpha} & I_F^{\alpha} & I_R & I_T^{\beta} & I_F^{\beta} \end{bmatrix} \tag{15}$$

$$\mathbf{V_S} = \begin{bmatrix} V_T^{\alpha} & V_F^{\alpha} & V_R & V_T^{\beta} & V_F^{\beta} \end{bmatrix} \tag{16}$$

$$\mathbf{Y_{PP}} = \begin{bmatrix} \frac{1}{Z_\alpha} & \frac{-1}{2Z_\alpha} & \frac{-1}{2Z_\alpha} \\ \frac{-1}{2Z_\alpha} & \frac{1}{4Z_\alpha} + \frac{1}{Z_\beta} & \frac{1}{4Z_\alpha} - \frac{1}{Z_\beta} \\ \frac{-1}{2Z_\alpha} & \frac{1}{4Z_\alpha} - \frac{1}{Z_\beta} & \frac{1}{4Z_\alpha} + \frac{1}{Z_\beta} \end{bmatrix} \tag{17}$$

$$\mathbf{Y_{PS}} = \mathbf{Y_{SP}^T} = \begin{bmatrix} \frac{-k_\alpha}{2Z_\alpha} & \frac{k_\alpha}{2Z_\alpha} & 0 & 0 & 0 \\ \frac{k_\alpha}{4Z_\alpha} & \frac{-k_\alpha}{4Z_\alpha} & 0 & \frac{-k_\beta}{2Z_\beta} & \frac{k_\beta}{2Z_\beta} \\ \frac{k_\alpha}{4Z_\alpha} & \frac{-k_\alpha}{4Z_\alpha} & 0 & \frac{k_\beta}{2Z_\beta} & \frac{-k_\beta}{2Z_\beta} \end{bmatrix} \tag{18}$$

$$\mathbf{Y_{SS}} = \begin{bmatrix} \frac{Z_1^{\alpha}+k_\alpha^2 Z_2^{\alpha}}{2Z_2^{\alpha}Z_\alpha} & \frac{Z_1^{\alpha}}{2Z_2^{\alpha}Z_\alpha} & \frac{-1}{Z_2^{\alpha}} & 0 & 0 \\ \frac{Z_1^{\alpha}}{2Z_2^{\alpha}Z_\alpha} & \frac{Z_1^{\alpha}+k_\alpha^2 Z_2^{\alpha}}{2Z_2^{\alpha}Z_\alpha} & \frac{-1}{Z_2^{\alpha}} & 0 & 0 \\ \frac{-1}{Z_2^{\alpha}} & \frac{-1}{Z_2^{\alpha}} & \frac{2}{Z_2^{\alpha}} + \frac{2}{Z_2^{\beta}} + \frac{-1}{r_g} & \frac{-1}{Z_2^{\beta}} & \frac{-1}{Z_2^{\beta}} \\ 0 & 0 & \frac{-1}{Z_2^{\beta}} & \frac{Z_1^{\beta}+k_\beta^2 Z_2^{\beta}}{2Z_2^{\beta}Z_\beta} & \frac{Z_1^{\beta}}{2Z_2^{\beta}Z_\beta} \\ 0 & 0 & \frac{-1}{Z_2^{\beta}} & \frac{Z_1^{\beta}}{2Z_2^{\beta}Z_\beta} & \frac{Z_1^{\beta}+k_\beta^2 Z_2^{\beta}}{2Z_2^{\beta}Z_\beta} \end{bmatrix} \tag{19}$$

In this study, the Scott transformer is modeled using multiple single-phase transformers, connected as represented in [32], through the PowerFactory software. The parameters of the Scott transformer model used in this paper are shown in Table 3, adapted from [28].

III. THE VIRTUAL INERTIA-INTEGRATED RAILWAY POWER CONDITIONER

The conventional RPC control strategy balances the load between both phases by transferring half of the difference in load power (ΔP_{RPC}) from the lower-demand phase to the higher-demand one, as indicated in (20). [16]

$$\Delta P_{RPC} = \frac{P_\alpha - P_\beta}{2} \tag{20}$$

where P_α and P_β represent the active power loads measured at the α and β phases, respectively. The RPC can also compensate for the reactive power load using (21).

$$\Delta Q_{\alpha/\beta,out} = K \cdot Q_{\alpha/\beta} \tag{21}$$

where $\Delta Q_{\alpha/\beta,out}$ refers to $\Delta Q_{\alpha,out}$ and $\Delta Q_{\beta,out}$, which are reactive power injection based on reactive loads measured at the α and β phases (Q_α and Q_β), respectively, and K is the compensation factor ranging from 0 to 1.

In this study, a full-bridge back-to-back RPC (FB-RPC) equipped with an ESS is considered. The proposed VIIRPC can be modeled as two dependent current sources that are controlled by three signals, as depicted in Fig. 6 and throughout (22)-(30). The VIIRPC can supply virtual inertia power (ΔP_{VI}) by utilizing an ESS installed at the DC link of the RPC, as shown in (22)-(24) and Fig. 1.

$$\Delta f = f_0 - f \tag{22}$$

$$\Delta P_{VI} = \frac{(sK_{VI} + D_{VI})}{R_{VI}} \cdot \Delta f \tag{23}$$

$$\Delta P_{VI} = \Delta P_{ESS} \tag{24}$$

where Δf is frequency different, f_0 is the reference frequency. f is the measured frequency. ΔP_{VI} is the virtual inertia power.

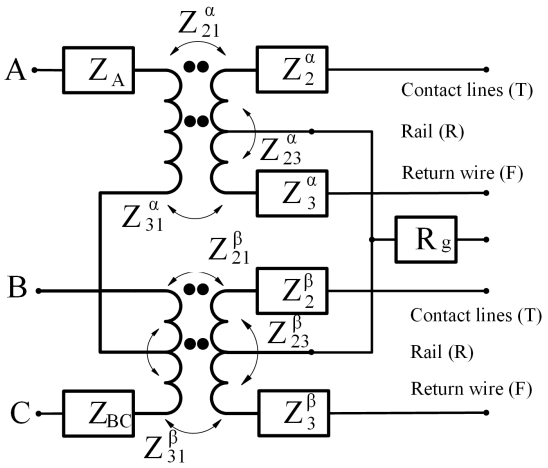

FIGURE 5. The scott transformer diagram.

TABLE 3. The parameters of Scott transformer model.

Parameters	Values
Rated Capacity (MVA)	60 (α+ β = 30+30)
Rated Voltage (kV)	α : 99.5929:50
	β : 115:50
Copper loss (kW)	α : 30
	β : 100
u_k (%)	α : 5.84%
	β : 10%

K_{VI} is the virtual inertia gain. D_{VI} is virtual damping gain. R_{VI} is the virtual inertia droop gain. Since the ESS is located on the secondary side of the Scott transformer, the virtual inertia control signal needs to be shared across both phases to maintain power balancing, similar to a conventional RPC, as shown in (25), where $\Delta P_{VI,h}$ is half the value of the signal.

$$\Delta P_{VI,h} = 0.5 \cdot \Delta P_{VI} \tag{25}$$

These shared signals are combined with each RPC control signal for the α and β phases, as shown in (26) and (27). These equations are based on a generator-oriented approach, in which a positive value indicates power supply, while a negative value indicates power consumption.

$$\Delta P_{VIRPC,\alpha} = \Delta P_{VI,h} + \Delta P_{RPC} \tag{26}$$

$$\Delta P_{VIRPC,\beta} = \Delta P_{VI,h} - \Delta P_{RPC} \tag{27}$$

The net active and reactive power can be calculated using (28) - (30).

$$P_{\alpha,net} = P_{\alpha} - \Delta P_{VIRPC,\alpha} \tag{28}$$

$$P_{\beta,net} = P_{\beta} + \Delta P_{VIRPC,\beta} \tag{29}$$

$$Q_{\alpha/\beta,net} = Q_{\alpha/\beta} - \Delta Q_{\alpha/\beta,out} \tag{30}$$

Two current sources shown in Fig. 6 are modeled using two static generators in PowerFactory. The control of these generators is achieved through $\Delta i_{dref,\alpha}$, $\Delta i_{dref,\beta}$, $\Delta i_{qref,\alpha}$, $\Delta i_{qref,\beta}$, and voltage angle ($\theta_{u,\alpha}$ and $\theta_{u,\beta}$) to inject $\Delta i_{1,\alpha}$ and $\Delta i_{1,\beta}$ as represented in (31)-(40) [33]. The control of the α phase side current source is achieved by using (31), in which the real and imaginary parts of $\Delta i_{1,\alpha}$ are illustrated in (32) and (33), respectively.

$$\Delta i_{1,\alpha} = \Delta i_{1,r,\alpha} + j\Delta i_{1,i,\alpha} \tag{31}$$

where

$$\Delta i_{1,r,\alpha} = \Delta i_{dref,\alpha} cos\theta_{u,\alpha} - \Delta i_{qref,\alpha} sin\theta_{u,\alpha} \tag{32}$$

$$\Delta i_{1,i,\alpha} = \Delta i_{dref,\alpha} sin\theta_{u,\alpha} + \Delta i_{qref,\alpha} cos\theta_{u,\alpha} \tag{33}$$

$$\Delta i_{dref,\alpha} = K_{id,\alpha} \cdot \Delta P_{VIRPC,\alpha} \tag{34}$$

$$\Delta i_{qref,\alpha} = K_{iq,\alpha} \cdot \Delta Q_{\alpha,out} \tag{35}$$

Similarly, the β phase side current source is controlled by utilizing equation (36), with the real and imaginary parts of $\Delta i_{1,\beta}$ being depicted in equations (37) and (38).

$$\Delta i_{1,\beta} = \Delta i_{1,r,\beta} + j\Delta i_{1,i,\beta} \tag{36}$$

where

$$\Delta i_{1,r,\beta} = \Delta i_{dref,\beta} cos\theta_{u,\beta} - \Delta i_{qref,\beta} sin\theta_{u,\beta} \tag{37}$$

$$\Delta i_{1,i,\beta} = \Delta i_{dref,\beta} sin\theta_{u,\beta} + \Delta i_{qref,\beta} cos\theta_{u,\beta} \tag{38}$$

$$\Delta i_{dref,\beta} = K_{id,\beta} \cdot \Delta P_{VIRPC,\beta} \tag{39}$$

$$\Delta i_{qref,\beta} = K_{iq,\beta} \cdot \Delta Q_{\beta,out} \tag{40}$$

The power-based signals obtained from (20)-(27) are transformed into current signals Δi_{dref} and Δi_{qref} for each α and β current source side. The control diagram of the VIIRPC is shown in Fig. 7. The power-current conversion for the α side is represented by (34) and (35), while the conversions for the β side are given by (39) and (40).

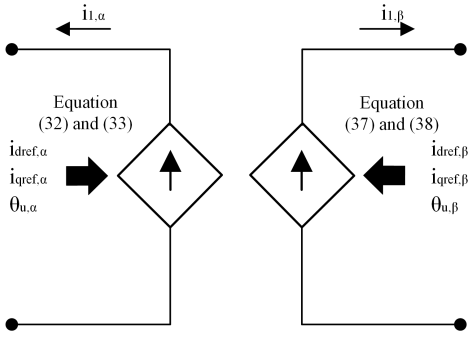

FIGURE 6. The current source model-based RPC.

IV. SIMULATION RESULTS

A. CASE STUDY

The evaluation of the proposed VIIRPC follows specific criteria outlined in Table 4, ensuring that frequency and voltage stay within 0.5% and 10% of their nominal values, respectively. Additionally, it ensures the voltage unbalance factor (VUF) remains below 2%, and the power factor (pf) is maintained close to unity. This evaluation encompasses two primary aspects: assessing operations under unbalanced and balanced loading conditions (CASE A1 and CASE A2), and simulating train operations with a 4-minute headway (CASE B1 to CASE B3).

For CASE 1 and CASE 2, the step load increases to 5 MW with a power factor (pf) of 0.95 at 1 second and decreases to zero at 61 seconds, as depicted in Fig 8. In the unbalanced condition (CASE A1), a step load is applied only to the β phase of the traction transformer. In contrast, for the balanced condition (CASE A2), identical step loads are applied to both α and β phases. These scenarios are examined under three conditions: without an RPC, with a conventional RPC, and with the VIIRPC, to compare their performances.

The evaluation of the VIIRPC's effectiveness is conducted through simulations covering three scenarios (CASE B1 to CASE B3). These simulations involve tracking the movement of trains on parallel tracks over a period of 800 seconds, utilizing the observed TPSS. The supply section's length for this TPSS has been established at 50 km, representing an average distance for 2 × 25 kV AT feeding systems, with the aim of maintaining the voltage level [34]. For this study, the CRH380A has been selected; it operates at a speed of 250 km/h, a velocity that is common in high-speed rail systems, as demonstrated in [35]. In this operating condition, the highest traffic density for a speed of 250 km/h in terms of "minute- headway" is 4 minutes. This headway can be calculated based on the proposal in [36], with a 20% safety margin. This traffic is selected and represented by a timetable diagram in Fig. 9, depicting two lines: the up-track (TU, in blue) and the down-track (TD, in red). Each line operates with a 4-minute headway for each train, and the up-track line is scheduled 2 minutes ahead of the down-track line.

In CASE B1, the impacts of traction load on conventional and low-inertia grids are compared in the study. In CASE

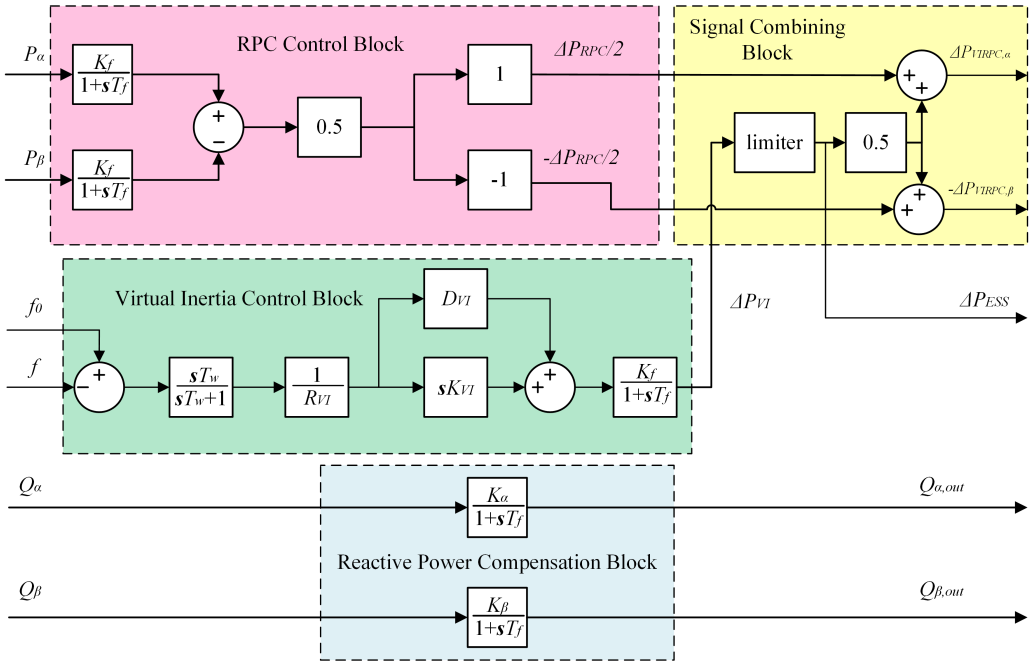

FIGURE 7. The VIIRPC control scheme.

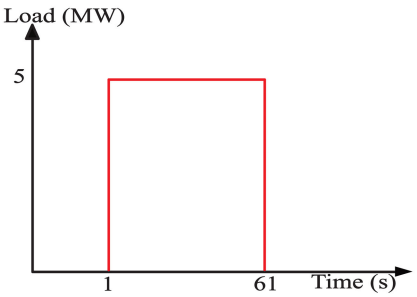

FIGURE 8. A 5 MW step-pulse load with 60 s width.

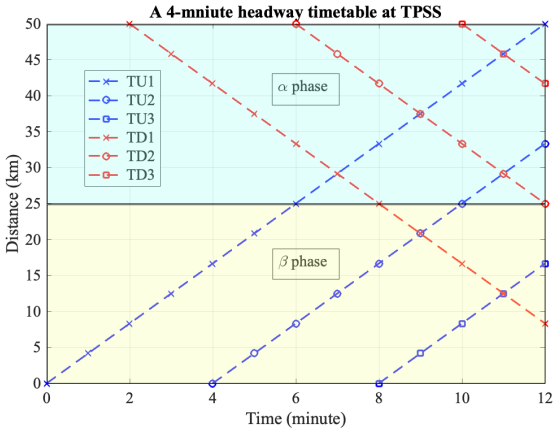

FIGURE 9. The 4-minute headway timetable at the observed TPSS.

B2, attention is given to the low-inertia power supply, and comparisons are made among the following sub-cases: before installation, with RPC installation, and with VIIRPC installation. CASE B3, which is similar to CASE B2, includes the examination of varying power supply conditions. Key cases and parameters are summarized in Tables 5 and 6. In Table 6, K_{VI} and D_{VI} are obtained through manual tuning across a range of load variations in time-domain simulations to guarantee the robustness of the controller. Firstly, the Δf signal is scaled up by the adjustment of R_{VI} to align the power output from both current sources with the traction loads. Given the presence of only two parameters within a narrow search space, they can be adjusted to achieve the expected response. Notably, K_α and K_β in Table 6 are negative, reflecting the inverse current injection directions of I_q (Q) and I_d (P).

TABLE 4. Research criteria.

Observed variables	Criteria
Frequency	Within 0.995 - 1.005 pu
Voltage	Within 0.90 - 1.10 pu
VUF	Less than 2%
pf	Approximate to 1

B. OPERATING MODE VERIFICATION

1) CASE A1: THE UNBALANCED CONDITION

The 5 MW step load with a 0.95 pf is connected to the β phase side of the Scott transformer. Upon detecting a load change, the VIIRPC responds by injecting active power into the β phase and absorbing active power from the α phase, as depicted in Fig. 10 (a). For a step-up change, the active

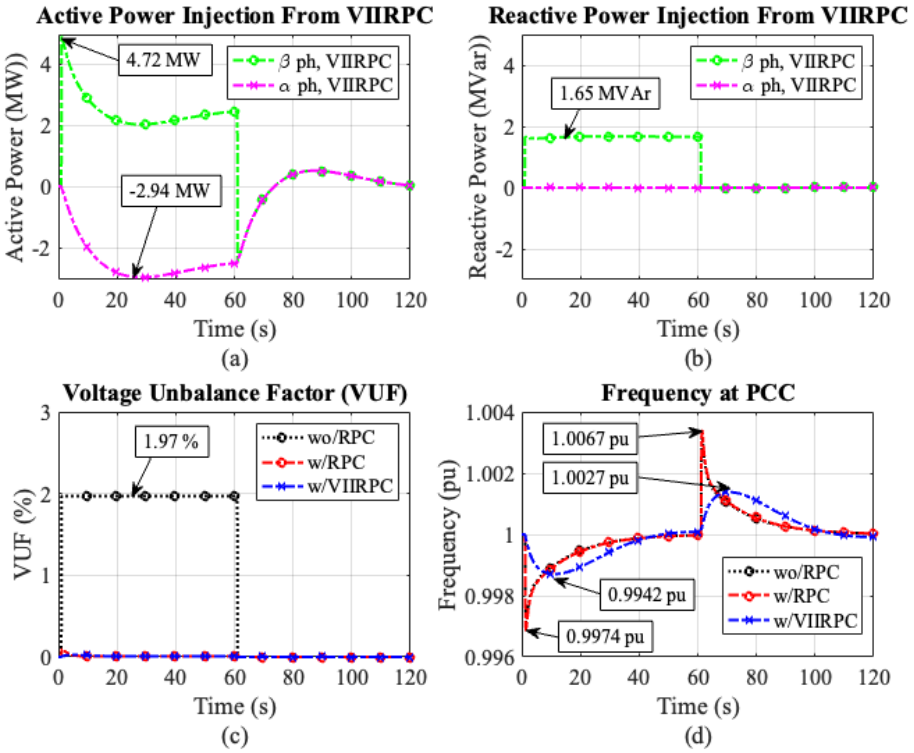

FIGURE 10. The CASE A1 results: a) active power, b) reactive power injection from the VIIRPC, c) VUF, and d) frequency deviation.

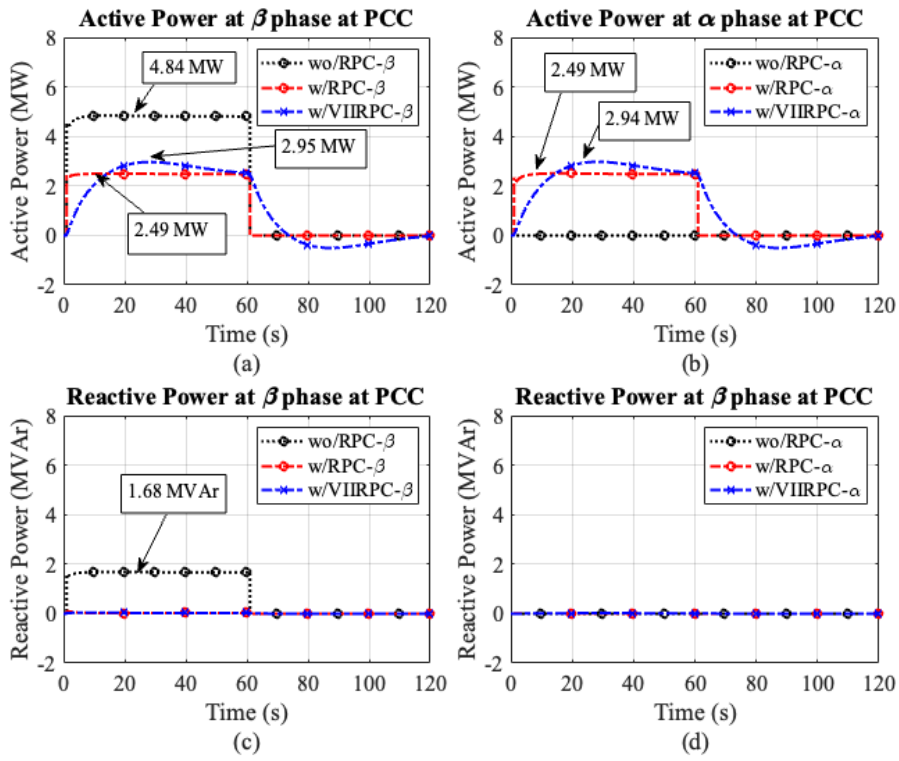

FIGURE 11. The load characteristics in CASE A1: without RPC, with RPC, and with VIIRPC installation case where a) the active power the β phase, b). the active power of the α phase, c) the reactive power load characteristic of the β phase, d) the reactive power of the α phase.

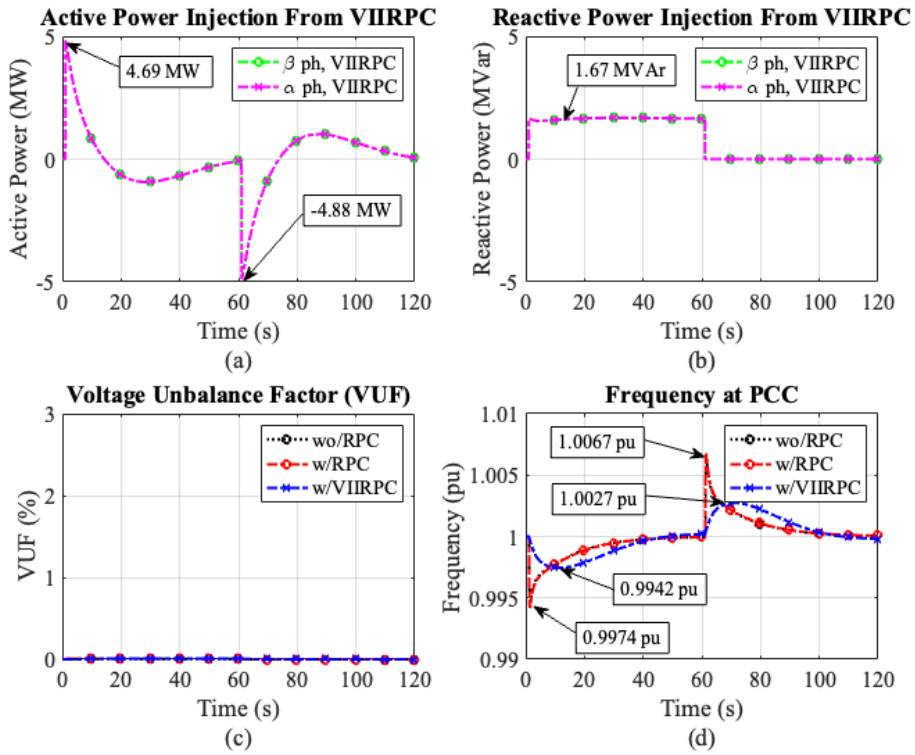

FIGURE 12. The CASE A2 results: a) active power, b) reactive power injection from the VIIRPC, c) VUF, and d) frequency deviation.

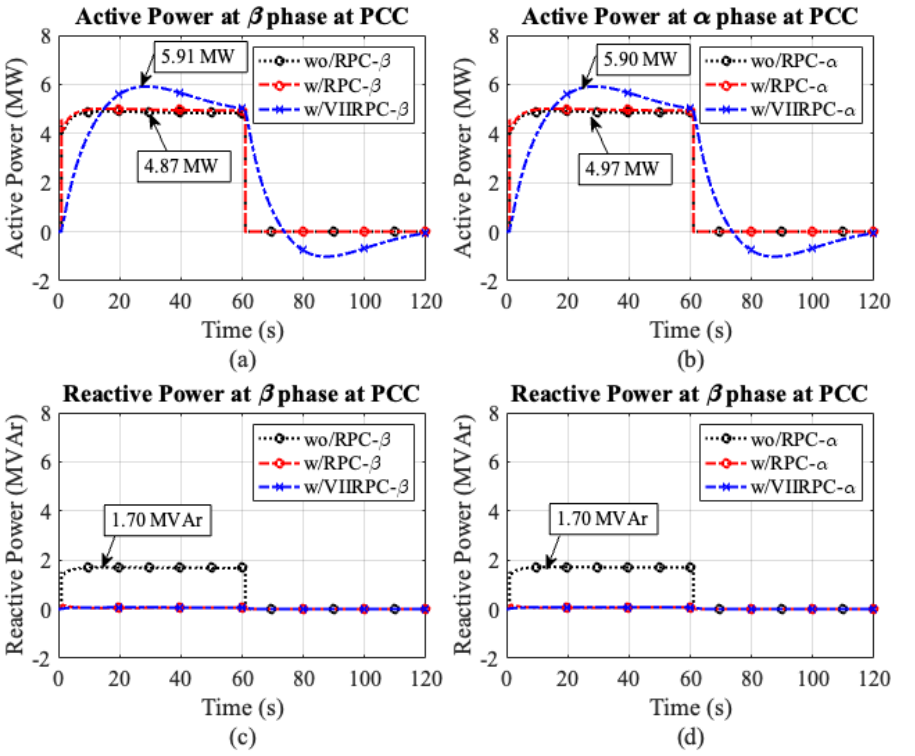

FIGURE 13. The load characteristics in CASE A2: without RPC, with RPC, and with VIIRPC installation case where a) the active power the β phase, b). the active power of the α phase, c) the reactive power load characteristic of the β phase, d) the reactive power of the α phase.

TABLE 5. Case study.

Case	Purpose	Approach	Simulation time (s)
A1	To verify the unbalanced condition	• Using a step-pulse load with pf 0.95 connected at β phase. • MVA_{sc} = 180 MVA, H = 0.01 s	120
A2	To verify the balanced condition	• Using two step-pulse load with pf 0.95 • MVA_{sc} = 180 MVA, H = 0.01 s	120
B1	To observe a low-inertia power supply impact	• convention grid with MVAsc = 870 MVA, H = 6 s and low-inertia grid with MVAsc = 180 MVA, H = 0.01 s • a 4-minute headway running trains as loads	800
B2	To evaluate VIIRPC performance	• low-inertia grid with MVAsc = 180 MVA, H = 0.01 s • a 4-minute headway running trains as loads	800
B3	As a case B2 with adding source variations	• As a case 4 with adding source variations	800

TABLE 6. Parameters setting of the VIIRPC.

Symbol	Value
K_f	1
T_f	0.01
R_{VI}	0.02
T_w	4
D_{VI}	5
K_{VI}	9
K_α	-1
K_β	-1
T_α	0.001
T_β	0.001

power injection at the β phase side consists of an inertial power (spike) offset by half of the active power load, while absorption at the α phase side is equal to half of the load minus the inertial power. Conversely, a step-down change triggers the absorption of inertial power (reversed spike) in both phases. Subsequently, the reactive power of this load is supplied by the β phase side of the VIIRPC, as shown in Fig. 10 (b). These VIIRPC behaviors contribute to the improvement of VUF and frequency deviation, illustrated in Fig. 10 (c) and 10 (d), respectively. The improvement shown in Fig. 10 (d), which includes RoCoF and frequency nadir, is summarized in Table 7.

The results are influenced by the change in load ramp-rate. In Fig. 11 (a) and (b), the active power characteristics of the β and α phases are compared across three scenarios: without RPC installation, with RPC installation, and with VIIRPC installation. In the scenario without an RPC, the β phase handles the entire 5 MW load, resulting in 1.97%

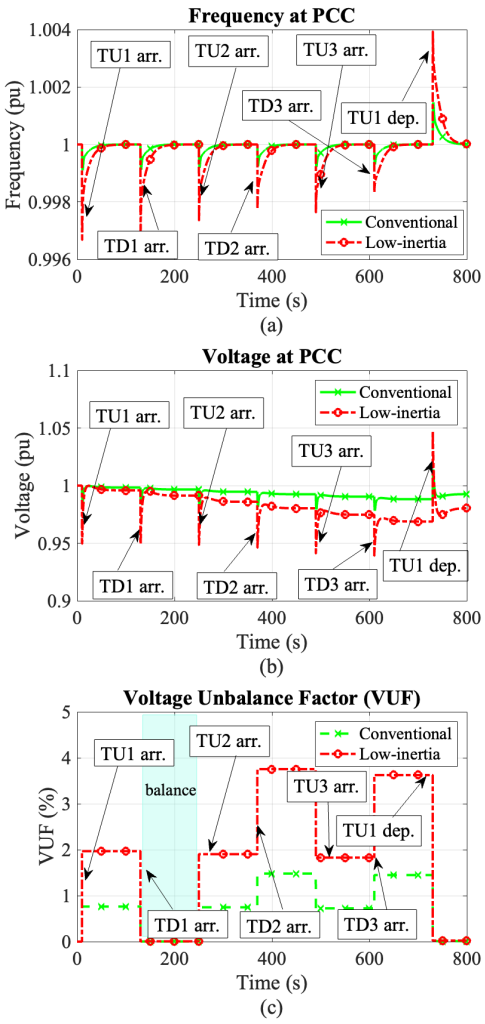

FIGURE 14. The comparison impacts from transitioning to a low-inertia power supply where a) frequency, b) voltage, and c) VUF.

TABLE 7. The comparison between RPC and VIIRPC (CASE A1).

Index	Step-up demand		Step-down demand	
	RPC	VIIRPC	RPC	VIIRPC
max-RoCoF (pu/s)	-3.3439	-0.1026	3.5550	0.1027
Frequency nadir (pu)	0.9968	0.9987	-	-
Frequency peak (pu)	-	-	1.0034	1.0014

VUF. After RPC installation, this active power is equally distributed to both phases, but frequency deviation issues persist. The installation of the VIIRPC addresses both unbalanced and frequency issues simultaneously by sharing the load equally and reducing the active power load ramp-rate. In Fig. 11 (c) and (d), the reactive power load is exclusively supplied by the β phase side converter.

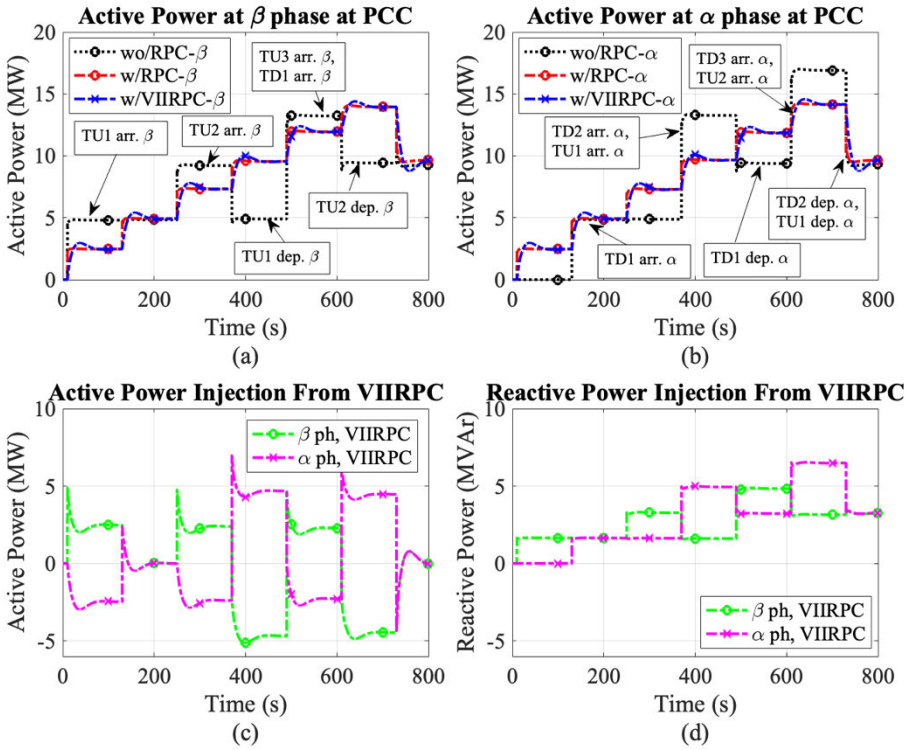

FIGURE 15. The Scott transformer load characteristic a) active power at β, b) active power at α, c) active power injection from the VIIRPC, and d) reactive power injection from the VIIRPC.

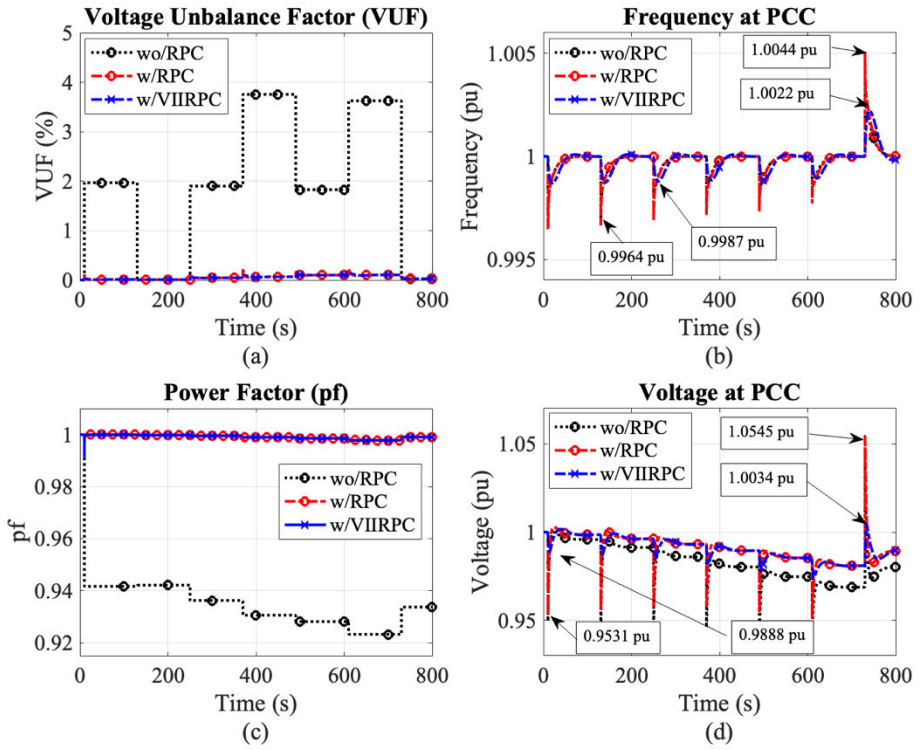

FIGURE 16. The VIIRPC results at PCC a) VUF b) bus frequency, c) power factor, and d) bus voltage.

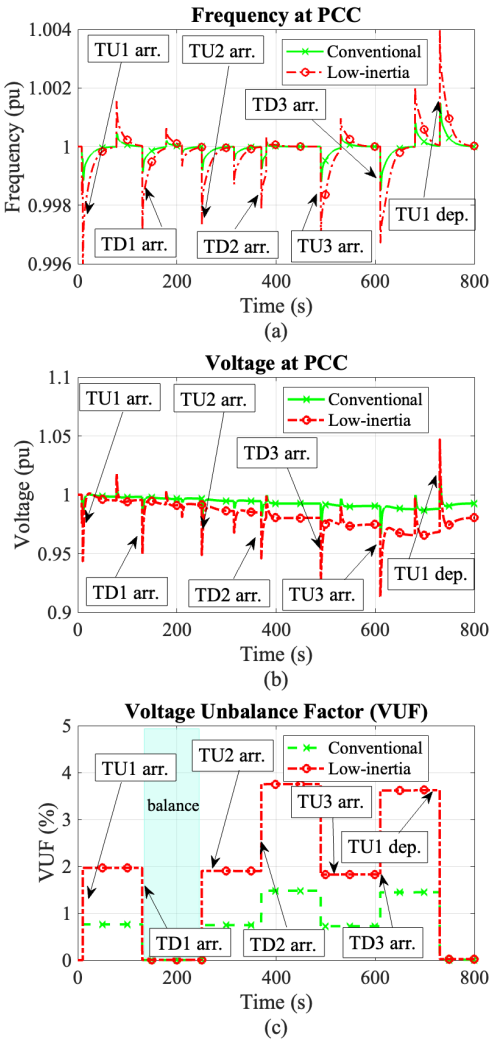

FIGURE 17. The fluctuating power supply characteristic without running trans where a) frequency, b) voltage, and c) VUF.

TABLE 8. The comparison between RPC and VIIRPC (CASE A2).

Index	Step-up demand		Step-down demand	
	RPC	VIIRPC	RPC	VIIRPC
max-RoCoF (pu/s)	-6.3040	-0.2057	7.0896	0.2044
Frequency nadir (pu)	0.9942	0.9975	-	-
Frequency peak (pu)	-	-	1.0067	1.0027

2) CASE A2: THE BALANCED CONDITION

The balanced condition is created using two 5 MW step loads with a 0.95 pf, connected to both secondary phases of the Scott transformer. In this scenario, as the load on the Scott transformer is already balanced, both sides of the VIIRPC provide only inertial power, as depicted in Fig. 12 (a). Each converter side fully supplies the reactive power load, as shown in Fig. 12 (b). Due to the balanced loading condition, the VUF is naturally eliminated, as indicated in Fig. 12 (c). However, frequency issues remain, triggering the virtual inertia control loop in the VIIRPC. The frequency deviation improvement, including RoCoF and frequency nadir demonstrations, is displayed in Fig. 12 (d) and summarized in Table 8.

Similar to CASE A1, the load ramp-rate for both phases is reduced during both step-up and step-down changes when the VIIRPC is installed, as shown in Fig. 13 (a) and (b). In these figures, the active power characteristics without RPC installation and with RPC installation are identical, indicating that the RPC control loop is not activated under balanced conditions. The reactive power for both phases is supplied by both sides, as demonstrated in Fig. 13 (c) and (d).

TABLE 9. The comparison between conventional and low-inertia power supply (CASE B1).

Index	Step-up demand		Step-down demand	
	Conv.	Low-H	Conv.	Low-H
max-RoCoF (pu/s)	-0.2769	-2.2802	0.4502	2.9632
Frequency nadir (pu)	0.9991	0.9967	-	-
Frequency peak (pu)	-	-	1.0015	1.0040
Voltage Min (pu)	0.9781	0.9390	-	-
Voltage Max (pu)	-	-	1.0141	1.0475

C. TRAIN RUNNING SIMULATION

In subsequent simulations, the highest traffic density scenario is established as mentioned earlier. The analysis is conducted in three parts: first, by comparing low-inertia and conventional railway power supplies (CASE B1); second, by evaluating the impact of the VIIRPC through a pre- and post-installation analysis (CASE B2); and third, by replicating the second scenario while incorporating the effects of power supply fluctuations (CASE B3).

1) CASE B1: LOW-INERTIA POWER SUPPLY IMPACTS

At the PCC of the TPSS, a comparison between conventional grids and RES-dominated grids is conducted, focusing on the impact of frequency, positive sequence voltage, and unbalance factor. These impacts are depicted in Fig. 14 (a)-(c), and RoCoF and frequency nadir are summarized in Table 9. During the simulation period, a total of 6 trains arrive at this TPSS, followed by the departure of TU1 at 730 seconds. Fig. 14 (c) shows a mix of unbalanced and balanced load conditions, with balanced conditions occurring during two intervals: 130 - 250 seconds, and the remainder being unbalanced. The results indicate that modern grids face challenges in managing a standard train operation schedule, failing to meet the specified criteria for these factors.

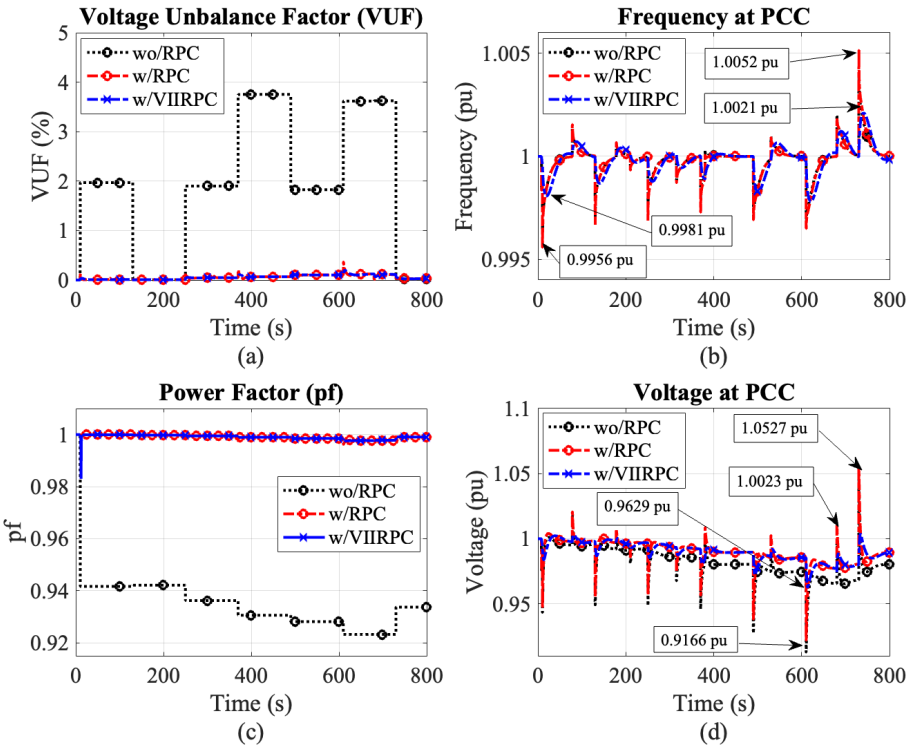

FIGURE 18. The VIIRPC results at PCC with power source fluctuations a) VUF b) bus frequency, c) power factor, and d) bus voltage.

TABLE 10. The comparison between RPC and VIIRPC (CASE B2).

Index	Step-up demand		Step-down demand	
	RPC	VIIRPC	RPC	VIIRPC
max-RoCoF (pu/s)	-2.4496	-0.0839	3.8497	0.1297
Frequency nadir (pu)	0.9964	0.9987	-	-
Frequency peak (pu)	-	-	1.0044	1.0022
Voltage Min (pu)	0.9531	0.9888	-	-
Voltage Max (pu)	-	-	1.0545	1.0034

TABLE 11. The comparison between RPC and VIIRPC (CASE B3).

Index	Step-up demand		Step-down demand	
	RPC	VIIRPC	RPC	VIIRPC
max-RoCoF (pu/s)	-4.0939	-0.1806	3.8468	0.1295
Frequency nadir (pu)	0.9956	0.9981	-	-
Frequency peak (pu)	-	-	1.0052	1.0021
Voltage Min (pu)	0.9166	0.9629	-	-
Voltage Max (pu)	-	-	1.0527	1.0023

2) CASE B2: A 4-MINUTE HEADWAY SCHEDULE CASE

In this study, the performance of the VIIRPC is compared with scenarios before any device installation and with a conventional RPC installation. The active power load characteristics for the β and α phases are shown in Fig. 15 (a) and (b). In Fig. 15 (a), the sequence of trains running through the β phase over 800 seconds is as follows: TU1 arrives at 10 seconds and departs at 370 seconds, TU2 arrives at 250 seconds and departs at 610 seconds, and TU3 and TD1 arrive at 490 seconds. In Fig. 15 (b), TD1 arrives at 130 seconds and departs at 370 seconds, TD2 and TU1 arrive at 730 seconds, and TD3 and TU2 arrive at 610 seconds. In both figures, the active power is a mix of unbalanced and balanced periods before any device installation. After the installation of RPC and VIIRPC, the active power is equally distributed between each phase. The notable difference between RPC and VIIRPC installations is the lower load ramp-rate in the VIIRPC case. For reactive power, each side supplies its own load separately, as discussed in CASE A1 and A2. The active and reactive power injection from the VIIRPC are shown in Fig. 15 (c) and (d).

The VIIRPC results, including VUF, frequency, power factor, and positive sequence voltage for this case, are displayed in Fig. 16 (a)-(d). These results demonstrate that the VIIRPC can eliminate VUF and maintain the power factor at unity, similar to a conventional RPC, while also helping to

TABLE 12. Geometry of the catenary system.

Circuit	1	2	3	4	5	6	7	8	9	10
X (m)	-2.7175	-1.2825	-2	-2	-5.5	1.2825	2.7175	2	2	5.5
Y (m)	1	1	8.3	6.3	9	1	1	8.3	6.3	9

improve frequency deviation aspects, which are summarized in Table 10.

3) CASE B3: A 4-MINUTE HEADWAY SCHEDULE WITH A FLUCTUATED POWER SOURCE CASE

In CASE B2, it is found that the VIIRPC is capable of operating effectively with a 4-minute headway train schedule under a consistent power supply. This section examines the impact of power supply fluctuations on its performance. Frequency, voltage, and VUF variations are shown in Figures 17 (a)-(c). Despite maintaining the same simulation parameters as the previous scenario, this iteration introduces a variable power source. The simulation results, including frequency, voltage, VUF, and pf, are depicted in Figures 18 (a)-(d). The VIIRPC's performance under fluctuating power conditions is summarized in Table 11, indicating effective operation even with power source variability.

V. CONCLUSION

In this paper, a novel VIIRPC control scheme is proposed, significantly augmenting the capabilities of conventional RPCs through the integration of virtual inertia support. A simplified yet comprehensive model for the VIIRPC, utilizing a current source-based framework, has been developed and presented. The model has been verified under a variety of load conditions, including both unbalanced and balanced conditions. The verification outcomes have confirmed that the VIIRPC effectively delivers inertia support, transitioning from an unbalanced system configuration (found on the secondary side of the Scott transformer) to a balanced three-phase system at the PCC. Further testing under a 4-minute headway train schedule, in both standard and low-inertia grid environments without initial RPC implementation, has underscored the challenges presented by low-inertia power systems. Following the installation of the VIIRPC, comparative simulations have been executed to assess scenarios with no RPC, existing RPC, and the newly introduced VIIRPC. These tests have demonstrated the VIIRPC's superior capability in enhancing the power system's performance, particularly in improving frequency stability, thereby surpassing traditional RPC solutions.

The theoretical explanation for the performance of the VIIRPC is that the acceleration of a frequency change, caused by a lack of inertia, can be counteracted by adopting a reverse perspective. This involves slowing the load change (load-ramp rate) through the injection of virtual inertia power, which is aimed at mitigating the frequency deviation, especially the RoCoF, and frequency nadir. While the primary design focus was on frequency support, the VIIRPC has also provided significant support in voltage stabilization, proving to be highly effective under the fluctuating conditions typical of variable power sources. The VIIRPC significantly benefits modern railway power supplies. Its value is crucial for TPSS in remote areas with greater dependence on RES. This paper demonstrates the application of VIIRPC to traction transformers, where the phasors on the secondary side are perpendicular, as observed in Scott transformers. This suggests the potential for broader adaptation across other types of transformers. Further research should explore the incorporation of railway systems to improve grid flexibility.

$$\mathbf{R} = \begin{bmatrix}
4.26\text{E}-01 & 4.92\text{E}-02 & 4.89\text{E}-02 & 4.89\text{E}-02 & 4.88\text{E}-02 & 4.92\text{E}-02 & 4.92\text{E}-02 & 4.88\text{E}-02 & 4.89\text{E}-02 & 4.88\text{E}-02 \\
4.92\text{E}-02 & 4.26\text{E}-01 & 4.89\text{E}-02 & 4.89\text{E}-02 & 4.88\text{E}-02 & 4.92\text{E}-02 & 4.92\text{E}-02 & 4.89\text{E}-02 & 4.89\text{E}-02 & 4.88\text{E}-02 \\
4.89\text{E}-02 & 4.89\text{E}-02 & 6.09\text{E}-01 & 4.86\text{E}-02 & 4.84\text{E}-02 & 4.89\text{E}-02 & 4.88\text{E}-02 & 4.85\text{E}-02 & 4.86\text{E}-02 & 4.84\text{E}-02 \\
4.89\text{E}-02 & 4.89\text{E}-02 & 4.86\text{E}-02 & 2.28\text{E}-01 & 4.85\text{E}-02 & 4.89\text{E}-02 & 4.89\text{E}-02 & 4.86\text{E}-02 & 4.86\text{E}-02 & 4.85\text{E}-02 \\
4.88\text{E}-02 & 4.88\text{E}-02 & 4.84\text{E}-02 & 4.85\text{E}-02 & 1.67\text{E}-01 & 4.88\text{E}-02 & 4.88\text{E}-02 & 4.84\text{E}-02 & 4.85\text{E}-02 & 4.84\text{E}-02 \\
4.92\text{E}-02 & 4.92\text{E}-02 & 4.89\text{E}-02 & 4.89\text{E}-02 & 4.88\text{E}-02 & 4.26\text{E}-01 & 4.92\text{E}-02 & 4.89\text{E}-02 & 4.89\text{E}-02 & 4.88\text{E}-02 \\
4.92\text{E}-02 & 4.92\text{E}-02 & 4.88\text{E}-02 & 4.89\text{E}-02 & 4.88\text{E}-02 & 4.92\text{E}-02 & 4.26\text{E}-01 & 4.89\text{E}-02 & 4.89\text{E}-02 & 4.88\text{E}-02 \\
4.88\text{E}-02 & 4.89\text{E}-02 & 4.85\text{E}-02 & 4.86\text{E}-02 & 4.84\text{E}-02 & 4.89\text{E}-02 & 4.89\text{E}-02 & 6.09\text{E}-01 & 4.86\text{E}-02 & 4.84\text{E}-02 \\
4.89\text{E}-02 & 4.89\text{E}-02 & 4.86\text{E}-02 & 4.86\text{E}-02 & 4.85\text{E}-02 & 4.89\text{E}-02 & 4.89\text{E}-02 & 4.86\text{E}-02 & 2.28\text{E}-01 & 4.85\text{E}-02 \\
4.88\text{E}-02 & 4.88\text{E}-02 & 4.84\text{E}-02 & 4.85\text{E}-02 & 4.84\text{E}-02 & 4.88\text{E}-02 & 4.88\text{E}-02 & 4.84\text{E}-02 & 4.85\text{E}-02 & 1.67\text{E}-01
\end{bmatrix}$$

$$\mathbf{X} = \begin{bmatrix}
9.88\text{E}-01 & 4.07\text{E}-01 & 3.11\text{E}-01 & 3.25\text{E}-01 & 3.01\text{E}-01 & 3.43\text{E}-01 & 3.23\text{E}-01 & 2.98\text{E}-01 & 3.07\text{E}-01 & 2.79\text{E}-01 \\
4.07\text{E}-01 & 9.88\text{E}-01 & 3.11\text{E}-01 & 3.25\text{E}-01 & 2.96\text{E}-01 & 3.71\text{E}-01 & 3.43\text{E}-01 & 3.04\text{E}-01 & 3.15\text{E}-01 & 2.86\text{E}-01 \\
3.11\text{E}-01 & 3.11\text{E}-01 & 7.86\text{E}-01 & 4.12\text{E}-01 & 3.51\text{E}-01 & 3.04\text{E}-01 & 2.98\text{E}-01 & 3.43\text{E}-01 & 3.40\text{E}-01 & 3.04\text{E}-01 \\
3.25\text{E}-01 & 3.25\text{E}-01 & 4.12\text{E}-01 & 7.67\text{E}-01 & 3.43\text{E}-01 & 3.15\text{E}-01 & 3.07\text{E}-01 & 3.40\text{E}-01 & 3.43\text{E}-01 & 3.02\text{E}-01 \\
3.01\text{E}-01 & 2.96\text{E}-01 & 3.51\text{E}-01 & 3.43\text{E}-01 & 7.22\text{E}-01 & 2.86\text{E}-01 & 2.79\text{E}-01 & 3.04\text{E}-01 & 3.02\text{E}-01 & 2.80\text{E}-01 \\
3.43\text{E}-01 & 3.71\text{E}-01 & 3.04\text{E}-01 & 3.15\text{E}-01 & 2.86\text{E}-01 & 9.88\text{E}-01 & 4.07\text{E}-01 & 3.11\text{E}-01 & 3.25\text{E}-01 & 2.96\text{E}-01 \\
3.23\text{E}-01 & 3.43\text{E}-01 & 2.98\text{E}-01 & 3.07\text{E}-01 & 2.79\text{E}-01 & 4.07\text{E}-01 & 9.88\text{E}-01 & 3.11\text{E}-01 & 3.25\text{E}-01 & 3.01\text{E}-01 \\
2.98\text{E}-01 & 3.04\text{E}-01 & 3.43\text{E}-01 & 3.40\text{E}-01 & 3.04\text{E}-01 & 3.11\text{E}-01 & 3.11\text{E}-01 & 7.86\text{E}-01 & 4.12\text{E}-01 & 3.51\text{E}-01 \\
3.07\text{E}-01 & 3.15\text{E}-01 & 3.40\text{E}-01 & 3.43\text{E}-01 & 3.02\text{E}-01 & 3.25\text{E}-01 & 3.25\text{E}-01 & 4.12\text{E}-01 & 7.67\text{E}-01 & 3.43\text{E}-01 \\
2.79\text{E}-01 & 2.86\text{E}-01 & 3.04\text{E}-01 & 3.02\text{E}-01 & 2.80\text{E}-01 & 2.96\text{E}-01 & 3.01\text{E}-01 & 3.51\text{E}-01 & 3.43\text{E}-01 & 7.22\text{E}-01
\end{bmatrix}$$

APPENDIX

A. GEOMETRY OF THE CATENARY SYSTEM

See Table 12.

B. IMPEDANCE MATRIX

R and **X**, as shown at the bottom of the previous page, are both represented in units of Ω/km.

REFERENCES

[1] P. Denholm, T. Mai, R. W. Kenyon, B. Kroposki, and M. O'Malley, "Inertia and the power grid: A guide without the spin," Dept. Nat. Renew. Energy Lab., Golden, CO, USA, Tech. Rep. NREL/TP-6120-73856, 6120. [Online]. Available: https://www.nrel.gov/docs/fy20osti/73856.pdf

[2] N. K. Roy, S. Islam, A. K. Podder, T. K. Roy, and S. M. Muyeen, "Virtual inertia support in power systems for high penetration of renewables—Overview of categorization, comparison, and evaluation of control techniques," *IEEE Access*, vol. 10, pp. 129190–129216, 2022, doi: 10.1109/ACCESS.2022.3228204.

[3] H. Bevrani, H. Golpîra, A. R. Messina, N. Hatziargyriou, F. Milano, and T. Ise, "Power system frequency control: An updated review of current solutions and new challenges," *Electr. Power Syst. Res.*, vol. 194, May 2021, Art. no. 107114, doi: 10.1016/j.epsr.2021.107114.

[4] T. Kerdphol, F. S. Rahman, M. Watanabe, and Y. Mitani, *Virtual Inertia Synthesis and Control*. Cham, Switzerland: Springer, 2021.

[5] L. Ali, M. I. Azim, J. Peters, V. Bhandari, A. Menon, V. Tiwari, J. Green, and S. M. Muyeen, "Application of a community battery-integrated microgrid in a blockchain-based local energy market accommodating P2P trading," *IEEE Access*, vol. 11, pp. 29635–29649, 2023, doi: 10.1109/ACCESS.2023.3260253.

[6] L. Ali, M. I. Azim, J. Peters, E. Pashajavid, V. Bhandari, A. Menon, V. Tiwari, and J. Green, "Local energy markets improve investment returns of residential BESS by arbitrage opportunities," in *Proc. IEEE Sustain. Power Energy Conf. (ISPEC)*, Dec. 2022, pp. 1–5, doi: 10.1109/iSPEC54162.2022.10032992.

[7] L. Ali, M. I. Azim, N. B. Ojha, J. Peters, V. Bhandari, A. Menon, J. Green, and S. M. Muyeen, "Integrating forecasting service and Gen2 blockchain into a local energy trading platform to promote sustainability goals," *IEEE Access*, vol. 12, pp. 2941–2964, 2024, doi: 10.1109/ACCESS.2023.3347432.

[8] P. Saxena, N. Singh, and A. K. Pandey, "Self-regulated solar PV systems: Replacing battery via virtual inertia reserve," *IEEE Trans. Energy Convers.*, vol. 36, no. 3, pp. 2185–2194, Sep. 2021, doi: 10.1109/TEC.2021.3052022.

[9] Q. Peng, Z. Tang, Y. Yang, T. Liu, and F. Blaabjerg, "Event-triggering virtual inertia control of PV systems with power reserve," *IEEE Trans. Ind. Appl.*, vol. 57, no. 4, pp. 4059–4070, Jul. 2021, doi: 10.1109/TIA.2021.3080227.

[10] T. Chen, J. Guo, B. Chaudhuri, and S. Y. Hui, "Virtual inertia from smart loads," *IEEE Trans. Smart Grid*, vol. 11, no. 5, pp. 4311–4320, Sep. 2020, doi: 10.1109/TSG.2020.2988444.

[11] X. Li, C. Zhu, and Y. Liu, "Traction power supply system of China high-speed railway under low-carbon target: Form evolution and operation control," *Electr. Power Syst. Res.*, vol. 223, Oct. 2023, Art. no. 109682, doi: 10.1016/j.epsr.2023.109682.

[12] Z. He, C. Wan, and Y. Song, "Frequency regulation from electrified railway," *IEEE Trans. Power Syst.*, vol. 37, no. 3, pp. 2414–2431, May 2022, doi: 10.1109/TPWRS.2021.3119706.

[13] Z. He, C. Wan, and Y. Song, "Adaptive frequency response from electrified railway," *IEEE Trans. Power Syst.*, vol. 38, no. 3, pp. 2880–2894, May 2023, doi: 10.1109/TPWRS.2022.3179369.

[14] W. Yu, Z. Liu, and I. A. Tasiu, "Virtual inertia control strategy of traction converter in high-speed railways based on feedback linearization of sliding mode observer," *IEEE Trans. Veh. Technol.*, vol. 70, no. 11, pp. 11390–11403, Nov. 2021, doi: 10.1109/TVT.2021.3112827.

[15] Y. Mochinaga, Y. Hisamizu, M. Takeda, T. Miyashita, and K. Hasuike, "Static power conditioner using GTO converters for AC electric railway," in *Proc. Conf. Rec. Power Convers. Conf.*, Yokohama, Japan, Apr. 1993, pp. 641–646, doi: 10.1109/PCCON.1993.264181.

[16] H. Morimoto, M. Ando, Y. Mochinaga, T. Kato, J. Yoshizawa, T. Gomi, T. Miyashita, S. Funahashi, M. Nishitoba, and S. Oozeki, "Development of railway static power conditioner used at substation for Shinkansen," in *Proc. Power Convers. Conf.*, vol. 3, Osaka, Japan, Apr. 2002, pp. 1108–1111, doi: 10.1109/pcc.2002.998127.

[17] S. M. M. Gazafrudi, A. T. Langerudy, E. F. Fuchs, and K. Al-Haddad, "Power quality issues in railway electrification: A comprehensive perspective," *IEEE Trans. Ind. Electron.*, vol. 62, no. 5, pp. 3081–3090, May 2015, doi: 10.1109/TIE.2014.2386794.

[18] H. M. Roudsari, A. Jalilian, and S. Jamali, "Flexible fractional compensating mode for railway static power conditioner in a V/v traction power supply system," *IEEE Trans. Ind. Electron.*, vol. 65, no. 10, pp. 7963–7974, Oct. 2018, doi: 10.1109/TIE.2018.2801779.

[19] Z. Zhang, B. Xie, S. Hu, Y. Li, L. Luo, C. Rehtanz, and O. Krause, "Reactive power compensation and negative-sequence current suppression system for electrical railways with YNvd-connected balance transformer—Part I: Theoretical analysis," *IEEE Trans. Power Electron.*, vol. 33, no. 1, pp. 272–282, Jan. 2018, doi: 10.1109/TPEL.2017.2670082.

[20] B. Xie, Z. Zhang, Y. Li, S. Hu, L. Luo, C. Rehtanz, and O. Krause, "Reactive power compensation and negative-sequence current suppression system for electrical railways with YNvd-connected balance transformer—Part II: Implementation and verification," *IEEE Trans. Power Electron.*, vol. 32, no. 12, pp. 9031–9042, Dec. 2017, doi: 10.1109/TPEL.2017.2662379.

[21] Z. Sun, X. Jiang, D. Zhu, and G. Zhang, "A novel active power quality compensator topology for electrified railway," *IEEE Trans. Power Electron.*, vol. 19, no. 4, pp. 1036–1042, Jul. 2004, doi: 10.1109/TPEL.2004.830032.

[22] M. Tanta, J. G. Pinto, V. Monteiro, A. P. Martins, A. S. Carvalho, and J. L. Afonso, "Topologies and operation modes of rail power conditioners in AC traction grids: Review and comprehensive comparison," *Energies*, vol. 13, no. 9, p. 2151, May 2020, doi: 10.3390/en13092151.

[23] H. Hayashiya, S. Yokokawa, Y. Iino, S. Kikuchi, T. Suzuki, S. Uematsu, N. Sato, and T. Usui, "Regenerative energy utilization in a.c. traction power supply system," in *Proc. IEEE Int. Power Electron. Motion Control Conf. (PEMC)*, Varna, Bulgaria, Sep. 2016, pp. 1125–1130, doi: 10.1109/EPEPEMC.2016.7752152.

[24] G. Cui, L. Luo, C. Liang, S. Hu, Y. Li, Y. Cao, B. Xie, J. Xu, Z. Zhang, Y. Liu, and T. Wang, "Supercapacitor integrated railway static power conditioner for regenerative braking energy recycling and power quality improvement of high-speed railway system," *IEEE Trans. Transport. Electrific.*, vol. 5, no. 3, pp. 702–714, Sep. 2019, doi: 10.1109/TTE.2019.2936686.

[25] J. Chen, H. Hu, Y. Ge, K. Wang, and Z. He, "Techno-economic model-based capacity design approach for railway power conditioner-based energy storage system," *IEEE Trans. Ind. Electron.*, vol. 69, no. 5, pp. 4730–4741, May 2022, doi: 10.1109/TIE.2021.3084158.

[26] K. Mongkoldee and T. Kulworawanichpong, "Optimal sizing of AC railway power conditioner in autotransformer-fed railway power supply system," *Int. J. Electr. Power Energy Syst.*, vol. 127, May 2021, Art. no. 106628.

[27] *Technical Reference: Single Phase Two Winding Transformer*, DIgSILENT GmbH, Gomaringen, Germany, 2022.

[28] H. Hu, Z. He, K. Wang, X. Ma, and S. Gao, "Power-quality impact assessment for high-speed railway associated with high-speed trains using train timetable—Part II: Verifications, estimations and applications," *IEEE Trans. Power Del.*, vol. 31, no. 4, pp. 1482–1492, Aug. 2016, doi: 10.1109/TPWRD.2015.2472961.

[29] *Technical Reference: General Load*, DIgSILENT GmbH, Gomaringen, Germany, 2022.

[30] *Technical Reference: Overhead Line Constants*, DIgSILENT GmbH, Gomaringen, Germany, 2022.

[31] H. Hu, Z. He, X. Li, K. Wang, and S. Gao, "Power-quality impact assessment for high-speed railway associated with high-speed trains using train timetable—Part I: Methodology and modeling," *IEEE Trans. Power Del.*, vol. 31, no. 2, pp. 693–703, Apr. 2016, doi: 10.1109/TPWRD.2015.2472994.

[32] T. Boonlert and K. Hongesombut, "Comparison of voltage distortion impacts from high-speed railway systems connected to electrical grid under different special transformers," in *Proc. Int. Electr. Eng. Congr. (IEECON)*, Krabi, Thailand, Mar. 2018, pp. 1–4, doi: 10.1109/IEECON.2018.8712124.

[33] *Technical Reference: Static Generator*, DIgSILENT GmbH, Gomaringen, Germany, 2022.

[34] T. Uzuka, "Faster than a speeding bullet: An overview of Japanese high-speed rail technology and electrification," *IEEE Electrific. Mag.*, vol. 1, no. 1, pp. 11–20, Sep. 2013, doi: 10.1109/MELE.2013.2271839.
[35] S. Bharule, T. Kidokoro, and F. Seta, "Evolution of high-speed rail and its development effects: Stylized facts and review of relationships," in *Proc. ADBI Work. Paper*, Dec. 2019, pp. 1–28, doi: 10.2139/ssrn.3554834.
[36] Y. Zhang, "Calculation methods of minimal headway for high-speed railways," in *Proc. ICTE*, Sep. 2015, pp. 203–213.

TEERAPHON PHOPHONGVIWAT (Member, IEEE) was born in Kanchanaburi, Thailand. He received the B.Eng. and M.Eng. degrees in electrical engineering from the King Mongkut's Institute of Technology Ladkrabang (KMITL), Bangkok, Thailand, in 1999 and 2002, respectively, and the Ph.D. degree in electrical and electronic engineering from the Wolfson Centre for Magnetics, Cardiff University, Cardiff, U.K., in 2013. Since 2014, he has been a Lecturer with the Department of Electrical Engineering, School of Engineering, KMITL, where he is currently an Assistance Professor. His current research interests include electric road/rail vehicle, battery, transformer, electrical machines, the application and characterization of soft magnetic materials, finite element, and optimization techniques.

THUNWA BOONLERT (Student Member, IEEE) was born in Phetchaburi, Thailand, in 1993. He received the B.Eng. and M.Eng. degrees in electrical engineering from Kasetsart University (KU), in 2016 and 2018, respectively, where he is currently pursuing the Ph.D. degree in electrical engineering. From 2017 to 2019, he was a Research Assistant with the Department of Electrical Engineering. Since 2020, he has been a Researcher with KU. His research interests include the areas of power system analysis and railway systems.

KOMSAN HONGESOMBUT (Member, IEEE) received the B.Eng. and M.Eng. degrees in electrical engineering from the King Mongkut's Institute of Technology Ladkrabang (KMITL), Bangkok, Thailand, in 1997 and 1999, respectively, and the Ph.D. degree in electrical engineering from Osaka University, Osaka, Japan, in 2003. From 2003 to 2005, he was awarded a Postdoctoral Fellowship by Japan Society for the Promotion of Science (JSPS). As a Postdoctoral Fellow, he worked on power system monitoring by application of GPS synchronized by PMU with the Department of Electrical Engineering, Kyushu Institute of Technology, Japan. From 2005 to 2009, he was a specialist in power systems with the Research and Development Center, Tokyo Electric Power Company, Japan. Since 2010, he has been with the Department of Electrical Engineering, Kasetsart Univeristy, Bangkok, where he is currently an Associate Professor. His research interests include the areas of power system analysis and protection.